Proceedings of the 16th European Turbomachinery Conference (ETC16)
Turbomachinery, Fluid Dynamics and Thermodynamics,
March 24-28, 2025; Hannover, Germany

A comparative study of varying incidence angle effects on a low-Reynolds-number compressor cascade based on experiments, low-fidelity and high-fidelity numerical simulations

Michael Bergmann*[1], Christian Morsbach[1], Felix M. Möller[2], Björn F. Klose[2], Alexander Hergt[1], and Georgios Goinis[1]

[1]Institute of Propulsion Technology, German Aerospace Center (DLR), Linder Höhe, 51147 Cologne
[2]Institute of Test and Simulation for Gas Turbines, German Aerospace Center (DLR), Linder Höhe, 51147 Cologne

Abstract

The ongoing trend in modern turbomachinery design towards higher bypass ratios and smaller core engines results in locally reduced Reynolds number distribution in modern compressors. While previous compressor blades were mostly designed for high Reynolds number operating points, blade designs specific for lower Reynolds numbers are becoming increasingly important. However, these operating points are characterised by large regions of flow separation and high levels of unsteadiness, where standard numerical design tools such as Reynolds-averaged Navier-Stokes (RANS) simulations typically exhibit high uncertainties. This can lead to incorrect prediction of the effects of varying incidence angles. On the other hand, high-fidelity numerical tools such as large-eddy simulations (LES), which resolve most scales of the turbulent spectrum, are affordable for low Reynolds number operating points due to the reduced bandwidth of scales.

In this paper, we assess the capabilities of low- and high-fidelity numerical tools for predicting the effects of varying incidence angles for a linear compressor cascade at a Reynolds number of 150 000 and Mach number of 0.6 based on the inflow conditions. The comparison is supported by experiments carried out at the Transonic Casacade Wind Tunnel at the DLR in Cologne, which feature an incidence angle variation of plus/minus 5 degrees. Particular emphasis is put on the numerical setup to reproduce the cascade experiment, discussing the effects of spanwise domain size, axial-velocity density ratio and inflow turbulence. The effects of the incidence angle variation are studied on the basis of instantaneous and mean flow quantities with a focus on separation, transition and loss mechanisms.

Keywords: Large-eddy simulation, Discontinuous Galerkin, Compressor, Separation, Transition, Entropy generation

1 Introduction

Efficiency improvements are one key aspect to meet the challenging governmental requirements on climate-neutral aviation. The design trends towards even higher bypass ratios and, as a result of limited clearance underneath the aircraft wings, towards more powerful and smaller core engines. Besides more pronounced secondary flow effects, this also results in locally reduced Reynolds numbers ($\mathrm{Re} \approx 10^5$) in axial compressor stages. At these low Reynolds numbers, airfoil aerodynamics become critical and losses can increase due to laminar or turbulent boundary layer separation. The airfoil aerodynamics at these operating points can also be subject to long and unsteady separation bubbles on the suction and/or pressure side of the blade, transition from laminar to turbulent boundary layers and a significant vortex shedding depending on the incidence angle. At off-design conditions with increasing incidence angles, the load on the boundary layers rises, resulting in moderately higher losses. Eventually, the airfoil reaches a point where it can no longer achieve the required pressure rise, leading to flow separation on the suction side and a sharp increase in the loss coefficient. A similar trend occurs for negative incidence angles, where the risk of pressure-side separation grows. This behavior is characteristic of blades operating under subsonic conditions.

The state-of-the-art design methodologies for axial compressor blades, such as multi-fidelity optimization processes using RANS simulations as a 'high-fidelity' tool [1, 2], can become unreliable at off-design points. This is because RANS, despite being considered high-fidelity, susceptible to significant modelling uncertainties under challenging operating conditions, might lead to over-predicted profile losses and misrepresentation of parameter trends. For instance, Hergt et al. [3] demonstrated that while RANS performs well within the typical design range of high Reynolds numbers, it fails to accurately predict loss trends and the static pressure rise at lower Reynolds numbers.

Unlike RANS, scale-resolving simulations such as DNS and LES capture all or most of the turbulent scales, respectively, and thus benefit from significantly reduced modeling uncertainty. Numerous publications in recent years have demonstrated that these methodologies perform well for compressor and turbine cascades, and when properly configured, can be as reliable as experimental data [4–8]. Scale-resolving simulations are especially well suited to flows with a low Reynolds number as the required computational resources remain moderate [9] and, depending on the case and solver properties, LES can be performed within some hours of wall-clock time. In addition to that, LES allows for a more in-depth analysis of the flow due to the availability of the temporally and spatially-resolved flow field. Building on these advan-

*Corresponding author: michael.bergmann@dlr.de

Table 1: Cascade design parameters

Inflow Mach number Ma_1	0.60
Inflow Reynolds number Re_1	1.5×10^5
Inflow angle α_1	43 deg
Turbulence intensity Tu	0.5%
Chord length c	70mm
Pitch to chord ratio b/c	0.577
Height to chord ratio h/c	2.4
Stagger angle α_s	16.04 deg
AVDR	1.03

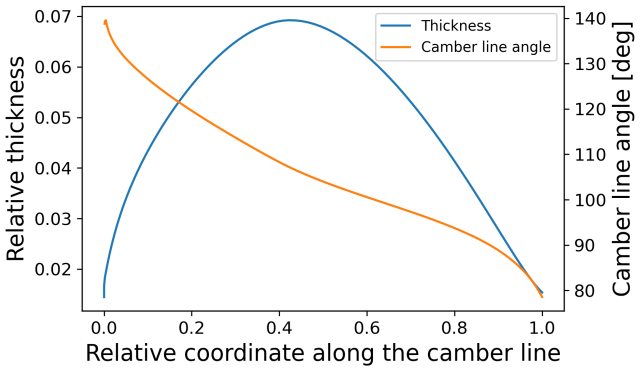

Figure 1: Profile thickness divided by the chord length and camber line angle

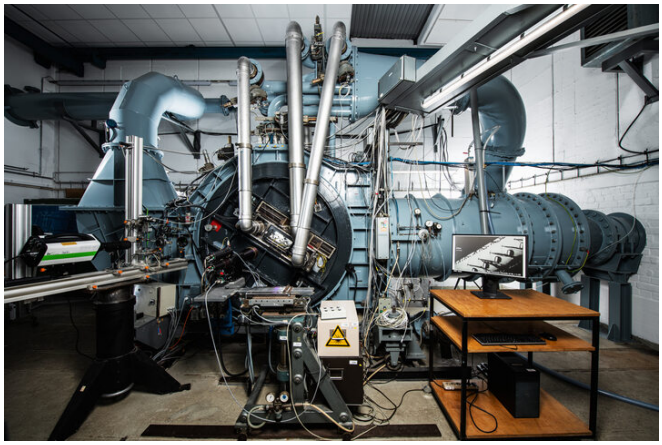

Figure 2: DLR's Transonic Cascade Wind Tunnel

tages, a modern high-order DG solver for LES and DNS has been developed within DLR's standard turbomachinery flow solver over the recent years [10, 11], which has been extensive validated on and applied for compressor and turbine cascade flows [6–8, 12, 13].

With the new high-fidelity tool at hand, we aim to reassess the cascade presented in Hergt et al. [3] and analyze the effects of the varying incidence angles on a modern compressor cascade at an operating point with a low Reynolds number of $\mathrm{Re}_1 = 1.5 \times 10^5$ and a Mach number of $\mathrm{Ma}_1 = 0.6$. The paper starts with a detailed description of the cascade, the experimental setup and both RANS and LES setups. The effects of the spanwise domain size, AVDR and inflow turbulence are discussed in terms of time- and space-averaged quantities obtained with LES for the zero-incidence-angle case. Subsequently, the results of different incidence angles, ranging from -5 deg to $+5$ deg, are compared between the experiment, RANS and LES. More detail on the loss production mechanisms is given by the analysis of entropy generation in the compressor flow field.

2 Cascade description

The compressor airfoil has originally been developed as an outlet guide vane behind a single low pressure turbine of a small turbofan engine [14, 15] and then been further optimized for the application of riblets [16]. An overview of the general design parameters is given in Tab. 1 and the profile thickness and camber line angle distribution in Fig. 1. The experiments were carried out in the Transonic Cascade Wind Tunnel [17, 18] at the DLR in Cologne. The numerical simulations, i.e. RANS and LES, have been performed with DLR's solver for turbomachinery flows TRACE, which is developed in close cooperation with MTU Aero Engines.

2.1 Experimental setup

The Transonic Cascade Wind Tunnel, as shown in Fig. 2, is a state-of-the-art facility for the study of compressor cascade flows, and has been developed for a long time to operate in difficult flow conditions. The wind tunnel is a closed loop facility and enables continuous testing. The test section is equipped with a variable nozzle. The variable test section height is necessary to adjust the test section on the specific cascades. Tailboards combined with throttles are used to control inlet and exit boundary conditions. In order to obtain tests at low Reynolds numbers, the total pressure in the closed loop system of the facility is reduced.

Within the experimental campaign, the cascade setup consists of 7 prismatic blades. Static pressure taps on the suction and pressure side surface at mid-span of blades number 3 and 5 are used to determine the profile Mach number distribution. In addition, measurement planes are located 20 mm in front of the blade's leading edge (MP1) and 20 mm behind its trailing edge (MP2). Conventional static pressure measurements are used at both planes. To derive the cascade loss, total pressure has been measured in the settling chamber as well as in the wake at MP2 by means of a 3-hole probe. Moreover, the AVDR in the cascade is controlled over boundary layer suction slots within the passages. Unfortunately, inflow turbulence was not measured during the present campaign, so we have to rely on previous measurements, which indicate turbulence intensity in the range of $\mathrm{Tu} = 0.3\% - 0.5\%$, with no available information on the turbulence length scale.

2.2 RANS setup

The RANS simulations are performed using a density-based Finite-Volume discretization on block-structured meshes. A MUSCL scheme with Van-Albada 1 limiter in combination with Roe's approximate Riemann solver is used to discretize

the convective fluxes and central derivatives are employed for the viscous fluxes to obtain second-order accuracy in space. In order derive the steady state solutions, the five conservation equations are solved in a coupled manner using an implicit dual time-stepping approach. The additional turbulence model equations are solved implicitly in a conservative but segregated manner [19]. In the present study, we employ Menter's SST k-ω model in the 2003 version [20] with stagnation point fix of Kato and Launder [21]. The transition from laminar to turbulent flow is modelled by the two-equation γ-Re_θ model [22]. This model combination represents a state-of-the-art setup in industrial turbomachinery CFD. At the inflow and outflow boundary conditions, two-dimensional non-reflecting boundary conditions are used [23]. Periodic boundary conditions are used in the pitchwise, and inviscid walls in the spanwise direction. The effect of the AVDR is modelled via a source term affecting the mass, momentum, and energy equations

$$S = \frac{1}{h}\frac{\partial h}{\partial x}\left([0,p,0,0,0]^T - F^x_{\mathrm{adv}}\right) \tag{1}$$

following Giles [24] and Bolinches et al. [25], where p is the static pressure, h the height of the channel, x the axial coordinate and F^x_{adv} the advective flux vector in the axial direction. The contraction of the channel height is modelled from the blade's leading edge towards the trailing edge and shaped with a sinusoidal distribution, i.e.

$$h(x) = \frac{h_{\mathrm{LE}} - h_{\mathrm{TE}}}{2}\left[\cos\left(\frac{x - x_{\mathrm{LE}}}{x_{\mathrm{TE}} - x_{\mathrm{LE}}}\pi\right) + 1\right] + h_{\mathrm{TE}}. \tag{2}$$

The same mesh has been used for all RANS simulations, which was created with the in-house meshing tool PyMesh using an O-C-H topology [26]. The mesh consists of 70480 hexahedral elements with one cell of height $\Delta\zeta = 0.002$m in the spanwise direction. For the ADP, a grid convergence index of 0.58% and the off-design point with +5 deg incidence angle 3.83% is reached on the integral total pressure loss coefficient. The domain and mesh are shown in Fig. 3. Probes are used to extract the mean flow values at several positions, i.e. MP1, MP2 or boundary layer cuts, ensuring consistency with the LES and experiment.

2.3 LES setup

The LES simulations have been performed with the high-order DG solver of TRACE, which has been developed over the recent years, thoroughly validated on and successfully applied to various turbomachinery-related configurations, cf. [6, 7, 10, 11, 13]. The implicitly filtered Navier-Stokes equations are first transformed into the reference system with a high-order polynomial mapping, which ensures free-stream preservation. The solution and fluxes are approximated via one-dimensional 4th-order Legendre polynomials with Legendre-Gauss-Lobatto basis nodes, which are extended to 3D in a tensor-product fashion. The numerical integration is performed with Legendre-Gauss-Lobatto quadrature, collocated with the solution approximation. The viscous terms are discretized using the Bassi and Rebay 1 scheme [27]. Adjacent elements are coupled via Roe's approximate Riemann solver

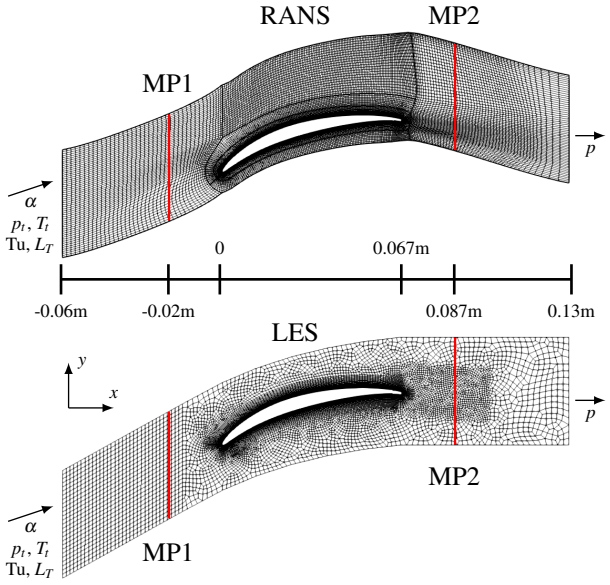

Figure 3: RANS and LES domain and mesh in the x-y plane. For the LES, only the high-order grid cells are shown and the solution nodes, i.e. 25 in each 2D element, are omitted for better visibility.

for the advective part and central fluxes for the viscous part. Stabilization for under-resolved turbulent flows is achieved by using a split formulation of the DGSEM following Gassner et al. [28]. In this present study, Kennedy-Gruber's kinetic-energy preserving two-point fluxes are used [29]. The resulting discretization achieves a 5th-order accuracy on unstructured hexahedral grids. The time-integration is performed by employing a strong-stability preserving third-order explicit Runge-Kutta scheme of Shu and Osher [30].

Riemann and one-dimensional non-reflecting boundary conditions are used at the inflow and outflow, respectively, cf. [23]. Inflow turbulence is generated synthetically at the inflow plane by an STG, originally proposed by Shur et al. [31], and implemented and validated in [32, 33]. The STG is based on a superposition of Fourier modes with random phases and direction vectors, which produce a modified von Karman spectrum. The fluctuations of the STG are added onto the boundary state derived from the boundary conditions and are weakly imposed over the flux. Periodicity is enforced in the pitch- and spanwise direction. Similar to RANS, the source term Eq. 1 is used to model the effect of the AVDR on the mid-section. The in- and outflow boundary values, i.e. total pressure $p_{t,\mathrm{in}}$, total temperature $T_{t,\mathrm{in}}$ and inflow angle α_{in} and the static pressure at the outflow p_{out} are set to the values measured in the experimental campaign of Hergt et al. [3].

The unstructured high-order mesh has been created as a 2D mesh with Gmsh [34], which was then uniformly extruded in the spanwise direction. In the x-y plane, the mesh consists of 10616 quadrilaterals. Polynomials of degree 2 have been used to approximate the curved boundary and the 6 layers adjacent to the wall. An overview of the 2D mesh can be found in Fig. 3, which clearly demonstrates benefit of unstructured meshes, being able to locally refine the mesh at relevant locations, i.e. boundary layer and wake region. In the spanwise

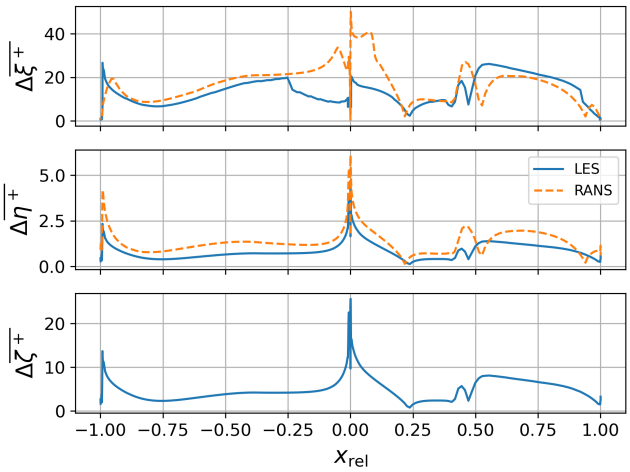

Figure 4: Non-dimensional cell sizes at the blade wall for RANS and LES at the aerodynamic design point. ξ is the wall-tangential, η the wall-normal and ζ the spanwise direction. For the LES, cell-sizes are divided by the polynomial degree N. The suction side is represented by positive values of x_{rel}, while the pressure side is represented by negative values.

direction, the resolution is kept constant for different spanwise extents, which is 24 elements and, hence, 120 DOF per $0.1c$.

Fig. 4 shows the non-dimensional cell sizes at the blade wall for the aerodynamic design point. The maximal cell sizes, i.e.

$$\Delta\overline{\xi^+} \leq 27.5,\ \Delta\overline{\eta^+} \leq 2.1,\ \Delta\overline{\zeta^+} \leq 12.2,\ \forall\, x_{\mathrm{rel}} \in (0.01, 0.99),$$

are well-below the limit of well-resolved LES [35]. Here, x_{rel} is the relative coordinate along the staggered blade, which is defined by

$$x_{\mathrm{rel}} = \cos\left(\arctan\left(\frac{y}{x}\right) - \alpha_s\right)\frac{\sqrt{x^2+y^2}}{c}, \tag{3}$$

where α_s is the stagger angle.

Each simulation is started from an initial RANS solution, which has been interpolated onto the fine high-order grid. The LES run for $43\,t_c$, defined by the inflow velocity and the chord length as $t_c = c/||\overline{u_1}||$. The line plots have been created with the time-resolved data of volume and boundary probes, which have been sampled with a frequency of $f_s = 10^6\,\mathrm{Hz} \approx 500/t_c$. The initial transient was automatically detected and removed by the MSER, cf. [36]. For entropy generation analysis, statistical moments of the full 3D flow field have been used, which have been sampled starting at $5t_c$ with same frequency as probes. The computational costs per convective time unit are 4 816.8 CPU/h, which corresponds to approximately 1.25 hours of wall-clock time on 3 840 CPUs.

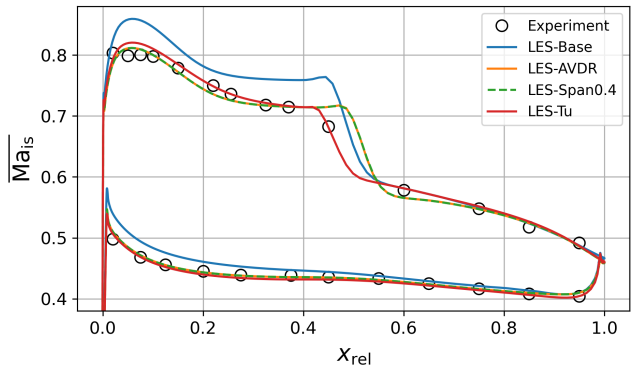

Figure 5: Time- and spanwise-averaged isentropic Mach number distribution around the blade.

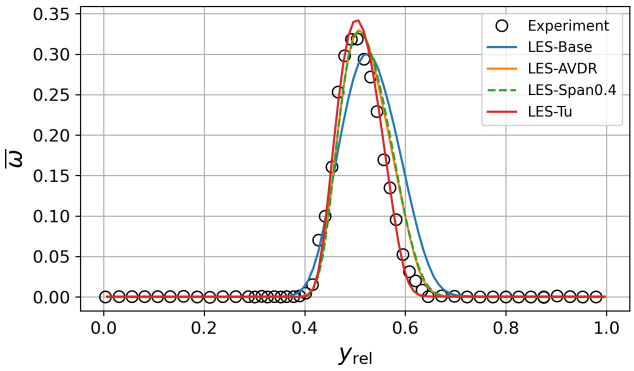

Figure 6: Time- and spanwise-averaged total pressure loss coefficient at the MP2.

3 Analysis of the LES setup for the aerodynamic design point

Before assessing the results of the incidence angle variation, the influence of different LES setup choices, namely the spanwise domain size, the AVDR and the inflow turbulence, are briefly discussed for the aerodynamic design point at $\alpha_1 = 43\,\mathrm{deg}$. For the setups listed in Tab. 2, the time- and spanwise-averaged isentropic Mach number and total pressure loss coefficients are shown in Fig. 5 and Fig. 6, respectively.

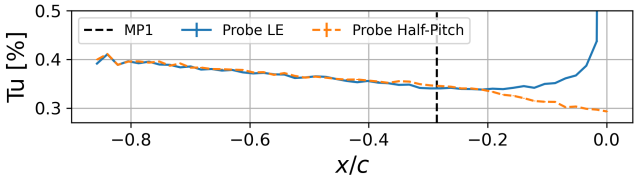

Figure 7: Turbulence intensity Tu along two inflow probes ($\alpha = 43\,\mathrm{deg}$) for *LES-Tu*. One probe was directed towards the leading edge and the other one has been moved by a half pitch towards the mid passage.

Table 2: Overview over the experimental and simulation parameters presented in section 3.

	Ma_1	Re_1	α_1 [deg]	Tu_1 [%]	L_T/c	AVDR	$\Delta z/c$	DOF [10^6]
Experiment	0.603	150791	43.0	0.3-0.5	-	1.0382	2.4	
LES-Base	0.630	155377	43.0	0	0	1	0.2	63.7
LES-AVDR	0.600	150294	43.0	0	0	1.0381	0.2	63.7
LES-Span0.4	0.600	150297	43.0	0	0	1.0380	0.4	127.5
LES-Tu	0.603	150833	43.0	0.33	0.01429	1.0381	0.2	63.7

The isentropic Mach number for the LES is computed as

$$\overline{\mathrm{Ma}_{\mathrm{is}}}(x_{\mathrm{rel}}) = \left\langle \sqrt{\frac{2}{\gamma-1}\left(\left(\frac{\langle \overline{p_{\mathrm{t},1}}\rangle}{\overline{p}(x_{\mathrm{rel}})}\right)^{\frac{\gamma-1}{\gamma}} - 1\right)} \right\rangle, \quad (4)$$

and the total pressure loss coefficient is computed as

$$\overline{\omega}(y) = \left\langle \frac{\langle \overline{p_{\mathrm{t},1}}\rangle - \overline{p_{\mathrm{t},2}}(y)}{\langle \overline{p_{\mathrm{t},1}}\rangle - \langle \overline{p_1}\rangle} \right\rangle. \quad (5)$$

The reference values are taken at the MP1. The wake coordinate is given by

$$y_{\mathrm{rel}} = (y - y_{\mathrm{LE}}) \bmod b. \quad (6)$$

Since the root location of the wake measurements could not be identified with certainty, the experiments are shifted to match the peak location of the *LES-Tu* in the ADP.

In addition to the LES results, the experimental results of Hergt et al. [3] are shown. Starting with the *LES-Base* without inflow turbulence and with an AVDR equal to 1, a significant difference in the Mach number distribution compared to the experiment can be observed. Clearly, the blade loading does not match, which is also visible in the increased Mach and Reynolds number at MP1, cf. Tab. 2. With the usage of the AVDR source term (*LES-AVDR*), although the effective flow area was only reduced by 3.8%, the loading does improve and, overall, the LES and the experiments converges. However, the length of the separation bubble on the suction side is significantly over-predicted. Doubling the spanwise domain size to $0.4c$ (*LES-Span0.4*) does not change the mean flow field and the isentropic Mach number and loss are identical. This can be also confirmed by the two-point correlation of the velocity components along the spanwise coordinate z, which exhibit a pronounced plateau at and above a span size of $0.2c$ (not shown). Hence, a span of $0.2c$ is assumed to be sufficient and will be used for the following LES.

The next parameter of uncertainty of the LES setup is the inflow turbulence, which has not been measured during the experimental campaign, but is known from previous studies in the wind tunnel without turbulence grids to be between 0.3% and 0.5%. We chose an inflow turbulence level at the CFD inlet of 0.4% with a turbulence length scale of $L_T = 0.001\,\mathrm{m}$, which fits 14 times into the spanwise domain. The distribution of the turbulence intensity along two inflow probes are shown in Fig. 7. Both are consistent until $x/c = -0.2$, where the potential field of the blade becomes significant. At MP1, the averaged turbulence intensity is $Tu_1 = 0.33\%$. The effect

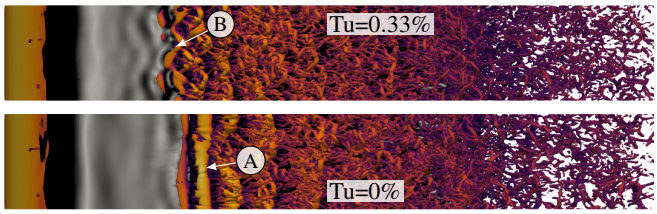

Figure 8: Instantaneous flow field on the suction side of the blade of *LES-AVDR* and *LES-Tu*. Q-isosurfaces colored by the velocity magnitude are shown in the volume and shear stress wall at the blade wall.

of free-stream turbulence can be studied by vortex visualisation of the instantaneous flow field close to the suction side of the profile in Fig. 8. Without inflow turbulence, one can observe the typical incoming laminar boundary layer, large mostly 2D Kelvin-Helmholtz roll-ups (A), which transition into 3D turbulence showing hairpin vortices. With inflow turbulence, even at the low level of Tu= 0.33%, the pronounced 2D roll-ups are not present anymore (B) and the transition and reattachment are shifted upstream. This can, of course, also be observed in the Mach number distribution shown in Fig. 5 The inflow turbulence significantly shortens the laminar separation bubble of the mean flow field by about 29%. This leads to a very good agreement with the experiment, matching the sensor data in nearly all locations, besides the most upstream ones very close to the leading edge. Due to the reduced size of separation, the wake loss profile also narrows towards the wake width of the experiment, cf. Fig. 6. The peak loss is slightly over-predicted, but, nonetheless, shows an overall remarkable agreement for such a sensitive quantity. It is worth noting that the inflow and outflow boundary conditions have been used directly from the experiment and were not tuned to match the operating point. Also the inflow turbulence is well in the given experimental range. With this setup and procedure, we will perform the variation of the inflow angle in the following section.

4 Incidence angle variation

In this section, the results from the experiments of Hergt et al. [3], RANS simulations and LES are compared for off-design conditions. Four additional incidence angles, i.e. $-5\,\mathrm{deg}$ ($\alpha_1 = 38\,\mathrm{deg}$), $-3\,\mathrm{deg}$ ($\alpha_1 = 40\,\mathrm{deg}$), $+3\,\mathrm{deg}$ ($\alpha_1 = 46\,\mathrm{deg}$) and $+5\,\mathrm{deg}$ ($\alpha_1 = 48\,\mathrm{deg}$), are considered and compared to the ADP. The inflow Mach number and Reynolds number are

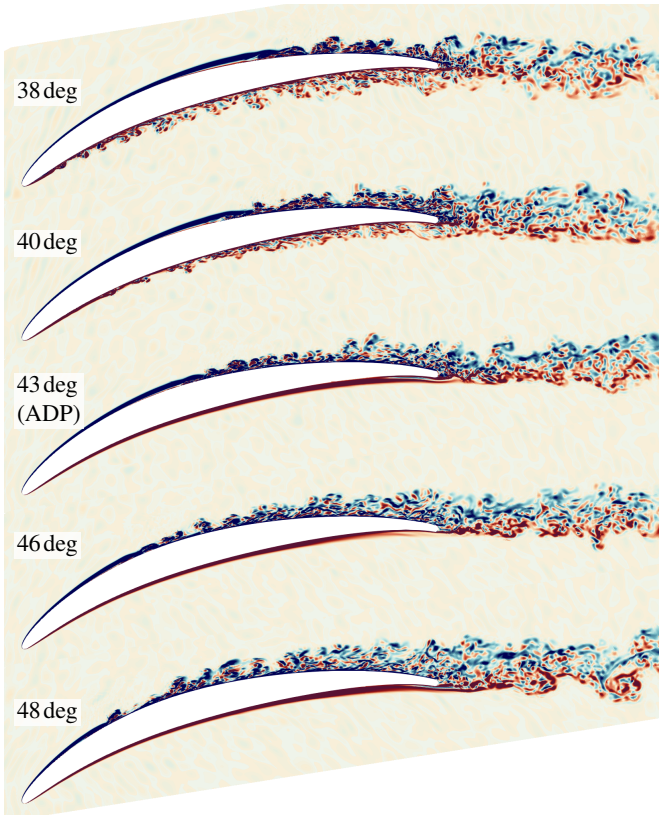

Figure 9: Instantaneous flow field at the mid span of the LES. The spanwise vorticity is shown. The illustrated pitch does not represent the original spacing used in the simulations, but is reduced for a better viability.

kept approximately constant over the angle variation. The in- and outflow boundary conditions for the simulations are taken from the experiment and are not adapted. The turbulent boundary conditions of RANS are tuned to match the one of the LES. The simulation parameters are shown in Tab. 3. Note that the experimental boundary conditions, i.e. total pressure, total temperature, and flow angles at the inflow, as well as static pressure at the outflow, are directly imposed to reproduce the setup as accurately as possible. Consequently, the Mach and Reynolds numbers at MP1 result from the predicted flow characteristics within the cascade. Hence, if the loss prediction differs significantly from the experiment, the inflow Mach and Reynolds numbers also change.

4.1 Instantaneous flow field

First, the instantaneous flow field of the different LES in Fig. 9 is analysed. The ADP ($\alpha_1 = 43\,\text{deg}$) is in the center of the figure, negative incidence is shown above and and positive incidence is shown below. At negative incidence, the laminar pressure side boundary layer occasionally separates for $\alpha_1 = 40\,\text{deg}$ and transitions at $x_{\text{rel}} \approx 0.14$. The highest negative incidence at $\alpha_1 = 38\,\text{deg}$ exhibits a separation fixed closely to the LE (9-A), resulting in a turbulent boundary layer over nearly the complete pressure side. This is also visualized in detail in Fig. 11. In the high-incidence case, typical 2D Kelvin-Helmholtz vortices are observed (11-A),

Table 3: Overview over the experimental and simulation parameters presented in section 4.

	Ma_1	Re_1	α_1 [deg]	Tu_1 [%]	AVDR
$\alpha = 38\,\text{deg}$, $j = -2$					
Exp	0.603	160 361	38.0	0.3-0.5	1.035
RANS	0.598	159 290	38.0	0.35	1.035
LES	0.603	160 379	38.0	0.35	1.036
$\alpha = 40\,\text{deg}$, $j = -1$					
Exp	0.602	151 992	40.0	0.3-0.5	1.024
RANS	0.595	151 127	40.0	0.36	1.024
LES	0.601	151 773	40.0	0.35	1.024
$\alpha = 43\,\text{deg}$, $j = 0$					
Exp	0.603	150 791	43.0	0.3-0.5	1.038
RANS	0.595	149 443	43.0	0.35	1.038
LES	0.603	150 833	43.0	0.33	1.038
$\alpha = 46\,\text{deg}$, $j = +1$					
Exp	0.600	147 764	46.0	0.3-0.5	1.032
RANS	0.590	145 862	46.0	0.35	1.032
LES	0.599	147 446	46.0	0.34	1.032
$\alpha = 48\,\text{deg}$, $j = +2$					
Exp	0.593	149 447	48.0	0.3-0.5	1.024
RANS	0.593	149 259	48.0	0.35	1.024
LES	0.608	152 002	48.0	0.38	1.024

which rapidly transition into a turbulent boundary layer characterized by large hairpin vortices. At moderate incidence angles (40 deg), the transition process is, however, delayed. Spanwise-correlated roll-ups develop near the leading edge and persist over a longer extent. These roll-ups eventually lead to the formation of lambda vortices (11-B) arising from instabilities within the separated shear layer. As the flow evolves, the shear layer becomes unstable, leading to the development of these vortex structures. The lambda vortices are precursors to further breakdown processes, which ultimately result in the formation of hairpin vortices (11-C) as the flow transitions into a fully turbulent boundary layer.

Looking at the suction side boundary layer in Fig. 9, the separation is delayed due to the reduced pressure gradient. Yet, when the boundary layer separates, even larger roll-ups occur (9-B) resulting in a thickening of the turbulent wake. With a positive incidence angle, the laminar boundary layer on the suction side separates earlier (9-C). The pressure side boundary layer remains laminar over the whole blade. However, the shape of the blade causes large-scale oscillations leading to large 2D structures in the wake (9-D).

4.2 Blade loading

In Fig. 10, the averaged isentropic Mach number is shown for all considered inflow angles of the experiment, LES and RANS simulations. The different incidence angles are shifted on the x-axis by their index j as noted in the text box, see Tab. 3. Overall, the agreement of both RANS and LES with the experiments is respectable. At the ADP, RANS predicts a very similar profile to the LES. Slight differences can be observed in the area of the suction side separation, where the reattachment position is delayed in the RANS. Moving to-

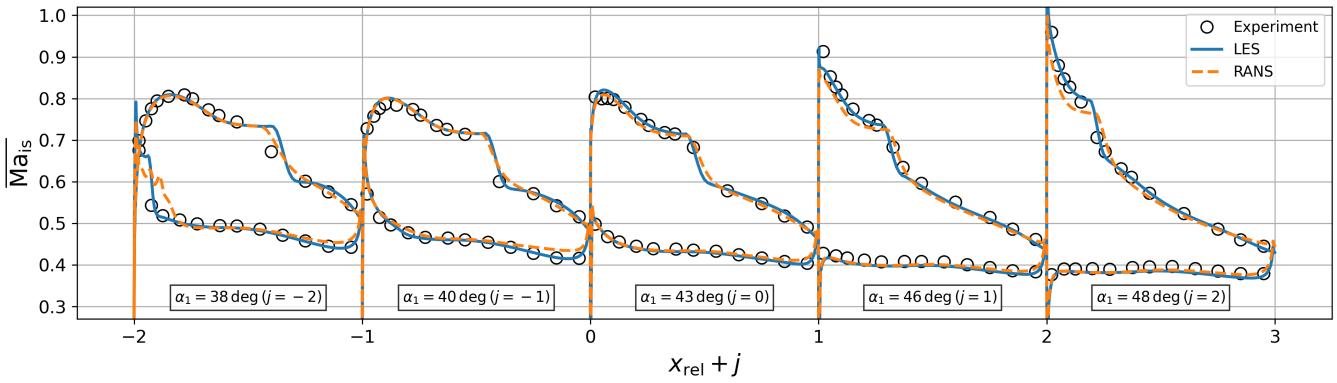

Figure 10: Isentropic Mach number distribution along the blade for different inflow angles.

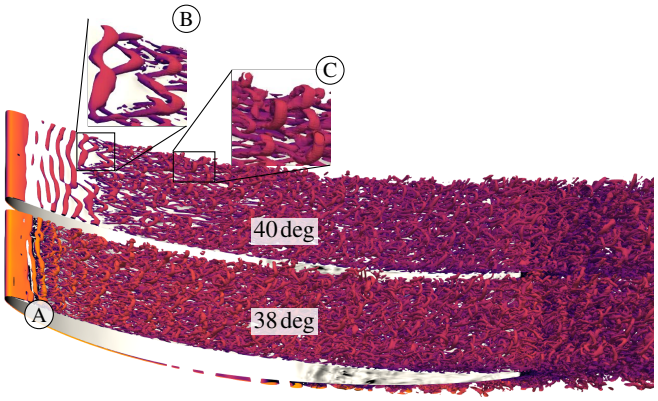

Figure 11: Isosurfaces of the Q-criterion coloured by the velocity magnitude on the blade's pressure side of the LES with $\alpha_1 = 38\,\mathrm{deg}$ and $\alpha_1 = 40\,\mathrm{deg}$.

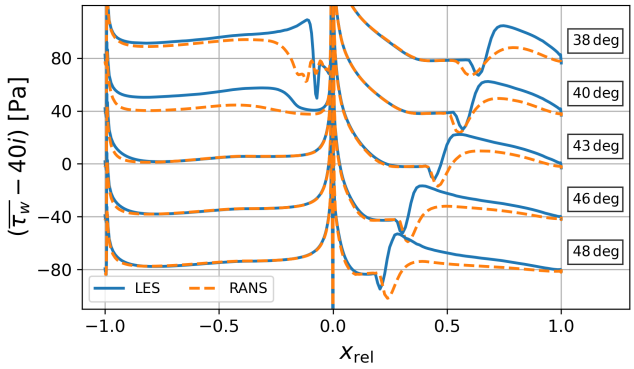

Figure 12: Time- and space-averaged wall shear stress along the blade for different inflow angles. The suction side is represented by positive values of x_{rel}, while the pressure side is represented by negative values.

wards positive incidence angles, this trend worsens. While the separation position is also advanced in RANS, the difference in size of the separation compared to LES is increased and to a higher pressure plateau. Looking at the negative incidence angles, the agreement with the experiment in terms of reattachment on the suction side is weakened. While the LES still decently matches the length of the bubble for $\alpha_1 = 40\,\mathrm{deg}$, it is significantly over-predicted for $\alpha_1 = 38\,\mathrm{deg}$. At this point, RANS seems to be closer to the experiment. Without further measurement data, the reason of the discrepancies are not clear. Inflow turbulence or inhomogeneous inflow boundary conditions could be an issue in the experiment. Yet, the pressure side separation is predicted well by the LES. Due to the pronounced unsteadiness in this region, RANS faces significant issues in reproducing the pressure distribution of the separation region, showing artificial oscillations.

4.3 Skin friction

The wall shear stress on the blade, shown in Fig. 12, underlines the observations made in the previous sections. It is defined as

$$\overline{\tau_w} = \mathrm{sign}\left(\langle\overline{\tau_{w,x}}\rangle\right) \cdot \sqrt{\langle\overline{\tau_{w,x}}\rangle^2 + \langle\overline{\tau_{w,y}}\rangle^2 + \langle\overline{\tau_{w,z}}\rangle^2}. \quad (7)$$

The separation onset, i.e. first zero crossing, is shifted downstream with decreasing inflow angles. Both, RANS and LES, agree on the location of separation while the prediction of the reattachment point differs. While for large inflow angles the separation size is larger in RANS due to a delayed transition, the difference decreases with smaller inflow angles, leading finally to a shorter separation bubble at $\alpha_1 = 38\,\mathrm{deg}$. Furthermore, the wall shear stress behind the reattachment is severely underpredicted by RANS compared to the LES.

On the pressure side, we can indeed discern a laminar boundary layer over the whole blade length at inflow angles $\alpha_1 \geq 43\,\mathrm{deg}$. At a moderate negative incidence angle, we observe the largest discrepancies between the LES and RANS. While no mean separation can be found in both LES and RANS, the laminar to turbulent transition and, hence, rapid increase of wall shear stress is not well predicted by RANS. This difference is preserved towards the TE. At the high negative incidence case, a pronounced, short separation bubble is present in the mean flow field, in which transition occurs. Although the transition is not well predicted by RANS, the difference in the wall shear stress past $x_{\mathrm{rel}} < -0.4$ is smaller than for $\alpha_1 = 40\,\mathrm{deg}$.

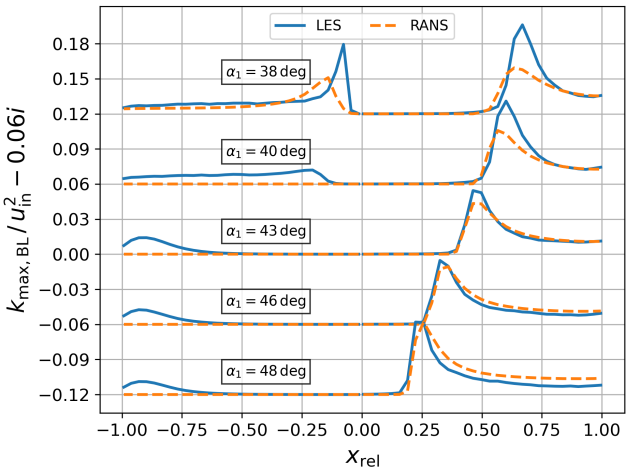

Figure 13: Maximal turbulent kinetic energy $k_{\mathrm{max,BL}}$ along boundary layer cuts on the suction ($+x_{\mathrm{rel}}$) and the pressure ($-x_{\mathrm{rel}}$) side. The position of the root point of the boundary layer cut on the blade surface determines the x value in the plot. The turbulent kinetic energy is normalized by the squared mean inflow velocity u_{in}^2.

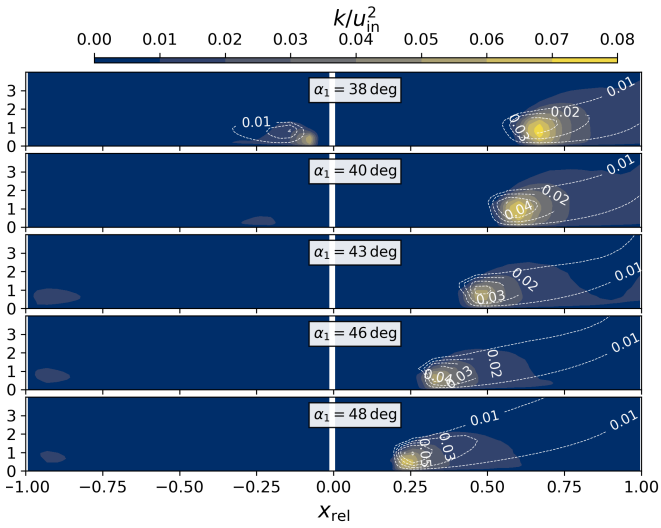

Figure 14: Turbulent kinetic energy k distribution along boundary layer cuts on the suction ($+x_{\mathrm{rel}}$) and the pressure ($-x_{\mathrm{rel}}$) side. The y-axis of each subplot represents the normalized wall distance $100\,d/c$, where c is the chord length and d is the distance to the wall. The results of LES are shown as coloured contours and the RANS results as white dotted contour lines.

4.4 Boundary layer analysis

To shed more light on the transition of the boundary layer, the maximum turbulent kinetic energy along several boundary layer cuts on the suction and pressure side is shown in Fig. 13. The differences on the pressure side are most obvious. One can confirm the observation made in the analysis of the wall shear stress that, for the near operating point at 38 deg, RANS predicts a significantly delayed transition. Similarly, the transition observed in the LES at 40 deg is not seen in RANS, which features a fully-attached, laminar boundary layer. Interesting observations can be also made close to the TE, where low-frequency oscillations occur for $\alpha_1 \geq 43\,\mathrm{deg}$. Certainly, these are not transition effects in the attached boundary layer, but rather oscillations of large-scale structures forming due to the profile shape. In Fig. 9 (D), their effect on the wake is also visible in the instantaneous flow field.

On the suction side, the differences between RANS and LES are the largest in the negative incidence cases. While the transition onset agrees fairly well, the level of turbulent kinetic energy behind reattachment differs significantly. With increased incidence angles, the differences in the level of turbulent kinetic energy reduces. It is, however, notable that, for positive incidence angles, RANS features a higher turbulent kinetic energy after transition, which seems to contradict the wall shear stress distribution in Fig. 12. However, when examining the distribution of turbulent kinetic energy along the boundary layer, as shown in Fig. 14, the maximum is closer to the wall in the LES. With approximately equal displacement thicknesses, the RANS exhibits a higher boundary layer momentum thickness compared to the LES, resulting in larger shape factors and reduced wall shear stress beyond the transition region on the suction side.

4.5 Conventional wake loss analysis

An important quantity for profile design is the profile loss coefficient. While there are multiple definitions of *the loss*, typically the total pressure loss is measured and investigated with the experiments [37]. Following Eq. (5), the total pressure loss of the experiment, RANS and LES for the considered inflow angles is shown in Fig. 15.

LES and experimental results agree exceptionally well in terms of both wake width and peak loss, except for the 48 deg case. Only the loss profile of this high incidence case exhibits notable discrepancies. The experiment shows higher total pressure loss on the suction side as the wake width increases, which is surprising since the isentropic Mach number distribution on the suction side aligns well with the LES, cf. Fig 10. Possible reasons for this discrepancy could be on both sides. On the one hand, inhomogeneous (in-)flow conditions might affect the results of the experiment, leading to certain blades being more heavily loaded. The experiment exhibits total pressure loss also in the suction side passage, which is neither found on the pressure side of the experiment, nor on the pressure and suction side passage in the RANS and LES results. On the other hand, although carefully setup, the LES might also exhibit some uncertainties. However, a simulation with two blades, i.e. the setup has been duplicated in the pitchwise direction, showed no effect on the total pressure loss. Furthermore, significant under-resolution of the LES is considered as rather unlikely, since virtually no turbulent structures propagate into the coarser wake region. On the chosen resolution, a grid convergence index of 0.40% for the integral loss of the +5 deg incidence case is reached. Additionally, a

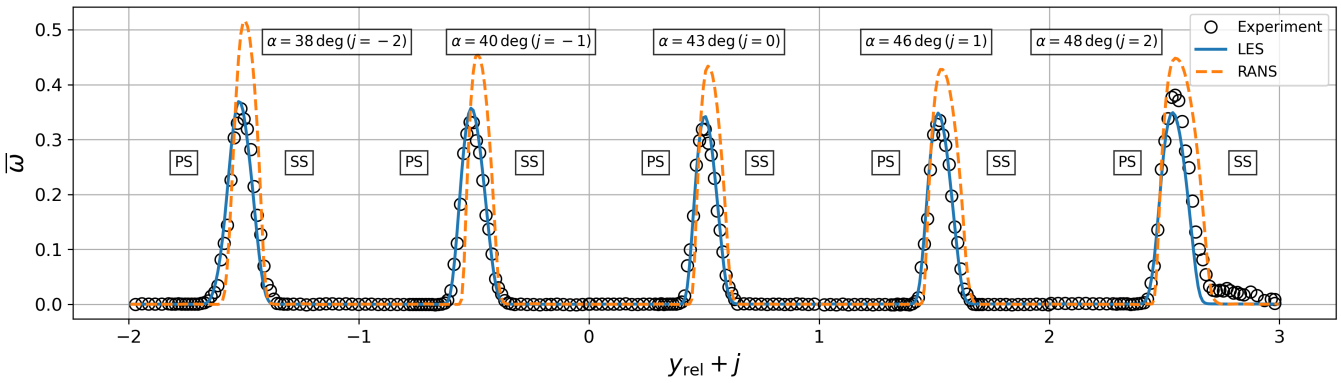

Figure 15: Time- and space-averaged total pressure loss coefficient $\overline{\omega}$ along the normalized pitchwise coordinate y_{rel} of MP2.

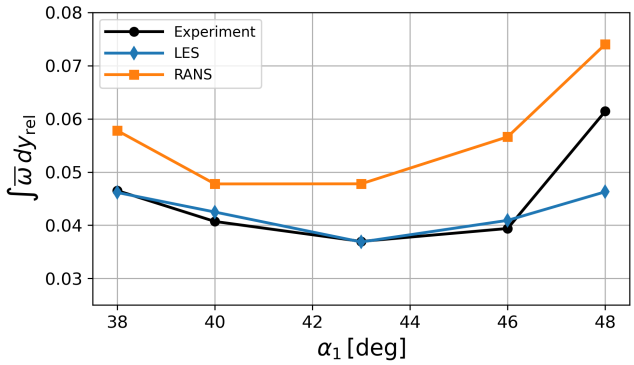

Figure 16: Pitchwise-integrated total pressure loss coefficient on MP2.

Table 4: Relative difference to the experimental integrated total pressure loss.

	38 deg	40 deg	43 deg	46 deg	48 deg
RANS	24.0%	17.3%	29.3%	43.7%	20.5%
LES	-0.8%	4.4%	-0.3 %	3.9%	-24.6%

high-order spatial discretization is employed, which is known for its excellent dispersion and dissipation properties, even at coarse grid resolutions [38]. A simulation with an extended structured zone around the blade and a refined outer wake region, totaling 7.0×10^6 DOF, affirms that there is virtually no difference in the total pressure loss (both not shown).

Comparing RANS with both other results, large discrepancies especially in the peak loss can be observed, which is known issue for RANS at lower Reynolds numbers, cf. [39–41]. For the positive incidence angles, the pressure side branch of the wake loss aligns well with the LES. Yet, the width towards the suction side is over-estimated. The effect could be related to the higher momentum thickness and more energetic boundary layer discussed in the previous section, which was especially present in the positive incidence case, cf. Fig. 14. At negative incidence angles, the pressure side seems to diverge from the LES and experiment, which could be linked to the discrepancies found in the separation and transition behavior.

In profile design optimizations, the shape of the loss profile is often irrelevant and only the integrated loss coefficient is considered. For that, flux-averaged or mixed-out quantities are analyzed. However, for the present experimental campaign, the definition of mixed-out quantities could not be comprehensibly applied to the RANS and LES data. Since, the mass flow was not available over the MP2 of the experiment, but all methodologies share the same position of MP2, we directly compare the *area*-integrated total pressure loss coefficient. Although we notice that the physical foundation of an area-averaged stagnation pressure is not given [42]. Fig. 16 shows the distribution over the inflow angle for RANS, LES and the experiments. RANS shows the expected offset. The largest difference of 43.7% is found to be with $\alpha_1 = 46\,\text{deg}$. Besides the high incidence case, in which elevated loss levels also occur in the passage, the LES agrees very well with the experiment, exhibiting relative differences below 5%.

Another important observation can be made here. RANS shows a disagreement regarding the optimal incidence angle compared to the findings from the LES and experimental results. Specifically, while the optimal inflow angle is identified as 43 deg for both the LES and the experiment, RANS does not align with this value. In traditional design paradigms, the primary focus is often on the general trend of the results rather than exact values. If the trend predicted by the model is correct, a small offset of loss in the optimal angle might be acceptable. However, in this case, the discrepancy in the optimal incidence angle represents a substantial issue. This deviation suggests that RANS does not accurately capture crucial aspects of the profile behavior for flows with low Reynolds numbers, which could impact the design and performance predictions.

4.6 Cascade deflection characteristics

Fig. 17 shows the deflection characteristics of the cascade for the different inflow angles. Clearly, the agreement between the experiment and LES is improved compared to RANS for this quantity, with a maximal difference of 0.68 deg. RANS shows a larger deviation from the experiment over the whole working range, underestimating the cascade deflection by about 2.4 deg at maximum. While this may not seem significant at first glance, in profile design optimization, where

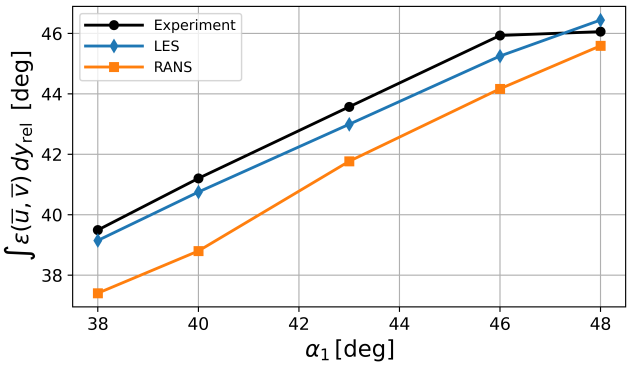

Figure 17: Pitchwise-integrated deflection angle ε at MP2.

flow deflection is often a restrictive constraint, the converged optimization results can fall outside the design constraints when re-evaluated with high-fidelity approaches or experiments. For the positive-incidence off-design point, both numerical deflection characteristics deviate from the experiment, which is most likely also linked to the increase of loss and uncertainties in the experimental setup observed and discussed in Fig. 16.

4.7 Entropy generation breakdown

In the previous section, disagreements of the profile loss predicted by RANS and LES have been found. However, the source of the difference is in many cases uncertain. While the analysis of boundary layer behaviour can offer some insights, a definite conclusions is often hard to be drawn. Exploiting the rich high-fidelity data, one methodology is based on the generation of entropy from the entropy balance equations, which was derived and analysed by Kock et al. [43] and Kock [44] or very recently in a slightly modified form for turbomachinery application [45, 46]. Ignoring the effects of temperature gradients and fluctuations, the main contributions for Favre-averaged entropy generation are [43]

$$\begin{aligned} g_s^{\text{mean}} &= \int_V \frac{1}{\widetilde{T}} \widetilde{\sigma_{ij}} \frac{\partial \widetilde{u_i}}{\partial x_j} dV \quad \text{and} \\ g_s^{\text{turbulent}} &= \int_V \frac{1}{\widetilde{T}} \overline{\sigma_{ij} \frac{\partial u_i''}{\partial x_j}} dV = \int_V \frac{1}{\widetilde{T}} \overline{\rho} \varepsilon dV, \end{aligned} \tag{8}$$

where V is the volume, $\widetilde{T}$ is the Favre-averaged temperature, σ_{ij} is the viscous stress tensor and $\overline{\rho}\varepsilon$ is the turbulent dissipation rate from the turbulent kinetic energy equation [47]. Equally, one could now replace the turbulent dissipation rate by the terms of the turbulent kinetic energy equation, cf. [45], but for the current paper the dissipation is used directly. Note that we only consider the resolved scales in the implicit LES, which is justified considering the high resolution of the present case. Furthermore, a decomposition of the domain into three different zones is performed following Raina et al. [48]:

- Suction side boundary layer with $d/c \leq 0.1$ and above the camber line

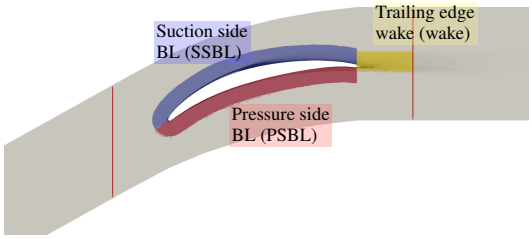

Figure 18: Zones of the entropy generation analysis on the ADP flow field. The total viscous dissipation is sketched in black.

- Pressure side boundary layer with $d/c \leq 0.1$ and below the camber line
- Trailing edge wake with $(\frac{\widetilde{T}\Delta\widetilde{s}}{\widetilde{u}^2} > 0.01 \cap |\widetilde{\omega}_{z'}| > |\widetilde{\omega}_{x'}| \cap |\widetilde{\omega}_{z'}| > |\widetilde{\omega}_{y'}|)$, where $\widetilde{\omega}$ is the vorticity vector and the prime coordinates represents the coordinate system rotated along the mean flow

The different zones are sketched in Fig. 18 for the LES of ADP.

The results of the spatial decomposition of the entropy generation mechanisms normalised with the total entropy generation of LES in the ADP are shown in Fig. 19. Several observations can be made from this. The first, which stands out the most, is that RANS overestimates the turbulent dissipation in the wake of the profile for all inflow angles, which can be linked to the overestimation of integral total pressure loss of shown in Fig. 16. In the suction side boundary layer, the agreement is better than in the wake. Nevertheless, the mean flow contributions of RANS for all incidence angles are lower than in LES, which is consistent with the lower wall shear stress on the suction side observed in Fig. 12. The trend of the turbulent contributions follows the wake observations, where the difference is especially pronounced in the highest positive incidence case (48 deg) with the integral turbulent dissipation rate more than doubled for RANS. Combined with the higher entropy generation in the wake, this seems to be a main factor for the large total pressure loss observed in Fig. 15. On the pressure side, a transitional boundary layer can be observed for decreasing inflow angles. Here, the turbulent content increases significantly at 40 deg and 38 deg, contributing to the overall entropy generation. In contrast, for RANS, turbulent dissipation is only observed at 38 deg, but not at 40 deg, highlighting its inability to correctly predict the transition on the pressure side.

5 Conclusions

This paper compares and analyses the effects of different incidence angles on the cascade's flow parameters, measured and simulated with RANS and LES at a Mach number of 0.6 and a Reynolds number of 150 000. The experimental campaign serves as the foundation of the analysis. The simulations use the in- and outflow boundary condition measured in the experiments as is, without relying on artificial tuning. Especially, note that RANS is using the same turbulent decay as the LES.

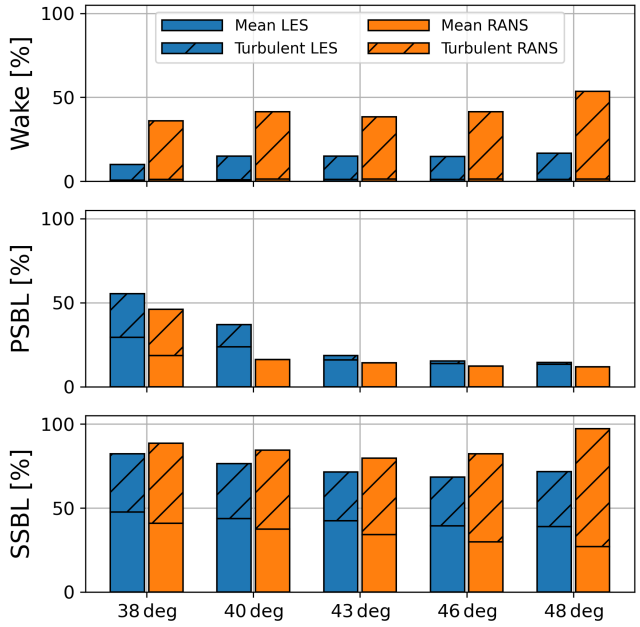

Figure 19: Mean and turbulent entropy generation contributions (Eq. 8) in three regions compared for RANS and LES for the five considered inflow angles α_1. The results are normalized by the total contribution of the LES in the ADP.

The analysis of the high-fidelity setup reveals a significant influence of the AVDR and the inflow turbulence. Ignoring the AVDR certainly results in different flow topology, shifting the total pressure loss towards the suction side. The influence of the inflow turbulence was surprising since the turbulence intensity is only about 0.3%. Yet, the laminar separation bubble seems to be susceptible to the perturbations, which reduce its length by 29%.

The findings from the study with five inflow angles can be summarized as follows. The agreement of the experiment and the LES is remarkable in terms of isentropic Mach number distribution and total pressure loss coefficients. Noticeable differences can only be found for the high positive incidence angle, where the loss on the suction side is higher in the experiment. Yet, the isentropic Mach number is well predicted by the LES. The accuracy of RANS with γ-Re_θ transition model for the considered cases is also considerable. Major effects can be quite well predicted, eg. the shift of the suction side separation and transition towards the leading edge for higher inflow angles or the transition occurring on the pressure side for the high negative incidence case with $\alpha_1 = 38\,\mathrm{deg}$. Nevertheless, deviations are still present, which can even negatively influence design decisions. Generally, RANS showed a significant deviation of the integral total pressure loss compared to the experimental results of at least 17.3%, but up to 41.1%. While a constant offset might be tolerable, trends should be correct. In contrast to the experiment and to the LES, the least integral loss was not predicted in the ADP, but at an inflow angle of 40 deg, i.e. $-2\,\mathrm{deg}$ incidence. Based on the comparison with LES in form of boundary layer analysis and entropy generation breakdown, this was linked to a failure to predict transition on the pressure side of the cascade and, hence, missing entropy generation from turbulent boundary layer. In addition, our analysis revealed that TKE profiles in the suction side boundary layer were thicker in RANS, i.e. having a higher momentum thickness compared to LES for all inflow angles and, therefore, higher suction side boundary layer loss. Moreover, the turbulent contribution to the generation inside the wake is also over-predicted by RANS for all incidence angles, which translates to the higher integral total pressure loss coefficient.

To conclude, the high-fidelity simulations using TRACE's DG solver demonstrate experimental-like accuracy for the considered compressor cascade flows at low-Reynolds-numbers conditions. The detailed data provided by LES allows for an in-depth analysis of differences compared to RANS, revealing limitations of the latter in predicting certain flow characteristics at these off-design conditions.

While it is difficult to establish a general guideline for designers based on this study, the main take-away is that the *uncertainties* introduced by RANS do not always result in a constant offset over the working range, but are flow dependent and especially pronounced in off-design conditions with an expected impact on working range predictions. This might lead to finding sub-optimal designs, which might even violate design constraints when being re-evaluated with experiments. With the increasing feasibility of high-fidelity scale-resolving simulations, particularly for low Reynolds number flows, LES offers a powerful tool for validating design predictions early in the development process. One step forward could be to adjust optimization constraints or targets based on the differences between LES and RANS for the baseline design. In future studies, we aim to leverage the high accuracy of LES in automated design optimization procedures, increasing fidelity levels and improving predictive capabilities at challenging operating points. This approach has the potential to enhance design reliability and reduce the reliance on experimental validation in early-stage development.

Acknowledgements

Michael Bergmann and Georgios Goinis would like thank the European Union for funding their research under grant number 101138080 (Project Sci-Fi-Turbo). Views and opinions expressed are however those of the author(s) only and do not necessarily reflect those of the European Union. Neither the European Union nor the granting authority can be held responsible for them.

Moreover, the authors gratefully acknowledge the scientific support and HPC resources provided by the German Aerospace Center (DLR). All simulations in this work have been carried out on the HPC system CARA which is partially funded by 'Saxon State Ministry for Economic Affairs, Labour and Transport' and 'Federal Ministry for Economic Affairs and Climate Action'.

Nomenclature

Ma	mach number
Re	Reynolds number
Tu	Turbulence intensity
b	pitch
c	chord length
d	distance to the wall
L_T	turbulence length scale
p	static pressure
p_t	stagnation (total) pressure
T	static temperature
t_c	convective time unit
V	volume
x, y, z	Cartesian coordinates

Greek symbols

α_1	inflow angle defined on the x-axis
α_s	stagger angle
Δ	cell size
ω	total pressure loss coefficient
σ	viscous stress tensor
τ	shear stress
ε	cascade deflection angle

Subscripts

1	values on the MP1
2	values on the MP2
i,j,k	Cartesian vector components
in	values on the CFD inlet
mean	contributions of the mean flow field
out	values on the CFD inlet
rel	relative values
turbulent	contributions of the turbulent fluctuations
w	value on the wall
x,y,z	Cartesian vector components

Superscripts

$\langle\square\rangle$	spanwise-averaged quantity $:= \frac{1}{\int_z dz}\int_z \square dz$
$\widetilde{\square}$	Favre-averaged quantity (temporally)
$\square''$	fluctuations from the Favre decomposition
$\overline{\square}$	Reynolds-averaged quantity (temporally)

Acronyms

ADP	aerodynamic design point
AVDR	axial-velocity-density-ratio
CFD	computational fluid dynamics
DG	discontinuous Galerkin
DGSEM	discontinuous Galerkin spectral element method
DNS	direct numerical simulation
DOF	degrees of freedom
FV	finite volume
LE	leading edge
LES	large-eddy simulation
MP	measurement plane
MSER	marginal standard error rule
RANS	Reynolds-averaged Navier-Stokes
STG	synthetic turbulence generator
TE	trailing edge

References

[1] C. Voß, M. Aulich, B. Kaplan, and E. Nicke. "Automated Multiobjective Optimisation in Axial Compressor Blade Design". In: vol. 6: Turbomachinery, Parts A and B. Turbo Expo: Power for Land, Sea, and Air. May 2006, pp. 1289–1297. DOI: 10.1115/GT2006-90420.

[2] C. Voß, S. Hemmert-Pottmann, and A. Schmitz. "Multi-fidelity optimization of a highly loaded low pressure compressor". In: The second European workshop on MDO for aeronautical industrial applications. Toulouse, Frankreich, 2019.

[3] A. Hergt, M. Pesch, S. Grund, and J. Flamm. "Low Reynolds Number Effects in Compressor Blade Design". In: *International Journal of Gas Turbine, Propulsion and Power Systems* 15.4 (2024). DOI: 10.38036/jgpp.15.4_v15n4tp08.

[4] V. Michelassi, L.-W. Chen, R. Pichler, and R. D. Sandberg. "Compressible Direct Numerical Simulation of Low-Pressure Turbines—Part II: Effect of Inflow Disturbances". In: *Journal of Turbomachinery* 137.7 (July 2015), p. 071005. DOI: 10.1115/1.4029126.

[5] J. Leggett, S. Priebe, A. Shabbir, V. Michelassi, R. Sandberg, and E. Richardson. “Loss Prediction in an Axial Compressor Cascade at Off-Design Incidences With Free Stream Disturbances Using Large Eddy Simulation”. In: *Journal of Turbomachinery* 140.7 (July 1, 2018), p. 071005. DOI: 10.1115/1.4039807.

[6] M. Bergmann, C. Morsbach, B. F. Klose, G. Ashcroft, and E. Kügeler. “A Numerical Test Rig for Turbomachinery Flows Based on Large Eddy Simulations With a High-Order Discontinuous Galerkin Scheme—Part I: Sliding Interfaces and Unsteady Row Interactions”. In: *Journal of Turbomachinery* 146.2 (Nov. 2023), p. 021005. DOI: 10.1115/1.4063734.

[7] C. Morsbach, M. Bergmann, A. Tosun, B. F. Klose, P. Bechlars, and E. Kügeler. “A Numerical Test Rig for Turbomachinery Flows Based on Large Eddy Simulations With a High-Order Discontinuous Galerkin Scheme—Part III: Secondary Flow Effects”. In: *Journal of Turbomachinery* 146.2 (Nov. 2023), p. 021007. DOI: 10.1115/1.4063511.

[8] B. F. Klose, C. Morsbach, M. Bergmann, E. J. Munoz Lopez, A. Hergt, and E. Kügeler. “The Unsteady Shock-Boundary Layer Interaction in a Compressor Cascade – Part 2: High-Fidelity Simulation”. In: vol. 12D: Turbomachinery — Multidisciplinary Design Approaches, Optimization, and Uncertainty Quantification; Radial Turbomachinery Aerodynamics; Unsteady Flows in Turbomachinery. Turbo Expo: Power for Land, Sea, and Air. June 2024. DOI: 10.1115/GT2024-124264.

[9] H. Choi and P. Moin. “Grid-point requirements for large eddy simulation: Chapman’s estimates revisited”. In: *Physics of Fluids* 24.1 (Jan. 2012), p. 011702. DOI: 10.1063/1.3676783.

[10] M. Bergmann, R. Gölden, and C. Morsbach. “Numerical investigation of split form nodal discontinuous Galerkin schemes for the implicit LES of a turbulent channel flow”. In: *7th European Conference on Computational Fluid Dynamics* (June 2018).

[11] M. Bergmann. “A split-form discontinuous Galerkin spectral element framework for scale-resolving simulations of turbomachinery flows”. doctoral thesis. Ruhr-Universität Bochum, Universitätsbibliothek, 2024. DOI: 10.13154/294-10845.

[12] M. Bergmann, C. Morsbach, and G. Ashcroft. “Assessment of Split Form Nodal Discontinuous Galerkin Schemes for the LES of a Low Pressure Turbine Profile”. In: *Direct and Large Eddy Simulation XII*. Ed. by M. García-Villalba, H. Kuerten, and M. V. Salvetti. Cham: Springer International Publishing, 2020, pp. 365–371. ISBN: 978-3-030-42822-8.

[13] B. F. Klose, C. Morsbach, M. Bergmann, A. Hergt, J. Klinner, S. Grund, and E. Kügeler. “A Numerical Test Rig for Turbomachinery Flows Based on Large Eddy Simulations With a High-Order Discontinuous Galerkin Scheme—Part II: Shock Capturing and Transonic Flows”. In: *Journal of Turbomachinery* 146.2 (Nov. 2023), p. 021006. DOI: 10.1115/1.4063827.

[14] T. Sonoda, Y. Yamaguchi, T. Arima, M. Olhofer, B. Sendhoff, and H.-A. Schreiber. “Advanced High Turning Compressor Airfoils for Low Reynolds Number Condition—Part I: Design and Optimization”. en. In: *Journal of Turbomachinery* 126.3 (Sept. 2004), pp. 350–359.

[15] H.-A. Schreiber, W. Steinert, T. Sonoda, and T. Arima. “Advanced High-Turning Compressor Airfoils for Low Reynolds Number Condition—Part II: Experimental and Numerical Analysis”. en. In: *Journal of Turbomachinery* 126.4 (Dec. 2004), pp. 482–492.

[16] A. Hergt, W. Hage, S. Grund, W. Steinert, M. Terhorst, F. Schongen, and Y. Wilke. “Riblet Application in Compressors: Toward Efficient Blade Design”. In: *Journal of Turbomachinery* 137.11 (Sept. 2015), p. 111006. DOI: 10.1115/1.4031090.

[17] W. Steinert, R. Fuchs, and H. Starken. “Inlet Flow Angle Determination of Transonic Compressor Cascades”. In: *Journal of Turbomachinery* 114.3 (July 1992), pp. 487–493. DOI: 10.1115/1.2929169.

[18] A. Hergt, J. Klinner, S. Grund, C. Willert, W. Steinert, and M. Beversdorff. “On the Importance of Transition Control at Transonic Compressor Blades”. In: *Journal of Turbomachinery* 143.3 (Mar. 2021), p. 031007. DOI: 10.1115/1.4049783.

[19] C. Morsbach and F. di Mare. “Conservative segregated solution method for turbulence model equations in compressible flows”. In: *6th European Congress on Computational Methods in Applied Sciences and Engineering (ECCOMAS 2012)*. 2012.

[20] F. Menter, M. Kuntz, and R. Langtry. “Ten years of Industrial experience with the SST model.” In: *Turbulence, Heat and Mass Transfer 4*. Ed. by K. Hanjalić, Y. Nagano, and M. Tummers. Jan. 2003, pp. 625–632.

[21] M. Kato and B. E. Launder. “The Modeling of Turbulent Flow Around Stationary and Vibrating Square Cylinders”. In: *9th Symposium on Turbulent Shear Flows*. 1993, pp. 10.4.1–10.4.6.

[22] R. B. Langtry and F. R. Menter. “Correlation-Based Transition Modeling for Unstructured Parallelized Computational Fluid Dynamics Codes”. In: *AIAA Journal* 47.12 (2009), pp. 2894–2906. DOI: 10.2514/1.42362.

[23] D. Schlüß, C. Frey, and G. Ashcroft. “Consistent Non-reflecting Boundary Conditions For Both Steady And Unsteady Flow Simulations In Turbomachinery Applications”. In: *ECCOMAS Congress 2016 VII European Congress on Computational Methods in Applied Sciences and Engineering, Crete Island, Greece*. 2016.

[24] M. Giles. *UNSFLO: A Numerical Method for the Calculation of Unsteady Flow in Turobmachinery*. Tech. rep. Gas Turbine Laboratory Report GTL 205, MIT Dept. of Aero. and Astro., 1991.

[25] M. Bolinches-Gisbert, D. C. Robles, R. Corral, and F. Gisbert. "Prediction of Reynolds Number Effects on Low-Pressure Turbines Using a High-Order ILES Method". In: *Journal of Turbomachinery* 142.3 (Feb. 2020), p. 031002. DOI: 10.1115/1.4045776.

[26] A. Weber and M. Sauer. *PyMesh - Template Documentation*. Technical report DLR-IB-AT-KP-2016-34. Linder Hoehe, Cologne, Germany: German Aerospace Center (DLR), Institute of Propulsion Technology, Feb. 2016.

[27] F. Bassi and S. Rebay. "A High-Order Accurate Discontinuous Finite Element Method for the Numerical Solution of the Compressible Navier–Stokes Equations". In: *Journal of Computational Physics* 131.2 (1997), pp. 267–279. ISSN: 0021-9991. DOI: https://doi.org/10.1006/jcph.1996.5572.

[28] G. J. Gassner, A. R. Winters, and D. A. Kopriva. "Split form nodal discontinuous Galerkin schemes with summation-by-parts property for the compressible Euler equations". In: *Journal of Computational Physics* 327 (Dec. 2016), pp. 39–66. DOI: 10.1016/j.jcp.2016.09.013.

[29] C. A. Kennedy and A. Gruber. "Reduced Aliasing Formulations of the Convective Terms Within the Navier-Stokes Equations for a Compressible Fluid". In: *Journal of Computational Physics* 227.3 (Jan. 2008), pp. 1676–1700. ISSN: 0021-9991. DOI: 10.1016/j.jcp.2007.09.020.

[30] C.-W. Shu and S. Osher. "Efficient implementation of essentially non-oscillatory shock-capturing schemes". In: *Journal of Computational Physics* 77.2 (Aug. 1988), pp. 439–471. DOI: 10.1016/0021-9991(88)90177-5.

[31] M. L. Shur, P. R. Spalart, M. K. Strelets, and A. K. Travin. "Synthetic Turbulence Generators for RANS-LES Interfaces in Zonal Simulations of Aerodynamic and Aeroacoustic Problems". In: *Flow Turbul. Combus.* 93.1 (2014), pp. 63–92. ISSN: 1573-1987. DOI: 10.1007/s10494-014-9534-8.

[32] C. Morsbach and M. Franke. "Analysis of a Synthetic Turbulence Generation Method for Periodic Configurations". In: *Direct and Large-Eddy Simulation XI*. Ed. by M. V. Salvetti, V. Armenio, J. Fröhlich, B. J. Geurts, and H. Kuerten. Cham: Springer International Publishing, 2019, pp. 169–174. ISBN: 978-3-030-04915-7.

[33] S. Leyh and C. Morsbach. "The Coupling of a Synthetic Turbulence Generator with Turbomachinery Boundary Conditions". In: *Direct and Large Eddy Simulation XII*. Ed. by M. García-Villalba, H. Kuerten, and M. V. Salvetti. Cham: Springer, 2020. Chap. 46. ISBN: 978-3-030-42822-8.

[34] C. Geuzaine and J.-F. Remacle. "Gmsh: A 3-D finite element mesh generator with built-in pre- and post-processing facilities". In: *International Journal for Numerical Methods in Engineering* 79.11 (2009), pp. 1309–1331. DOI: 10.1002/nme.2579.

[35] N. J. Georgiadis, D. P. Rizzetta, and C. Fureby. "Large-Eddy Simulation: Current Capabilities, Recommended Practices, and Future Research". In: *AIAA Journal* 48.8 (Aug. 2010), pp. 1772–1784. DOI: 10.2514/1.J050232.

[36] M. Bergmann, C. Morsbach, G. Ashcroft, and E. Kügeler. "Statistical Error Estimation Methods for Engineering-Relevant Quantities From Scale-Resolving Simulations". In: *Journal of Turbomachinery* 144.3 (Oct. 2021). 031005. DOI: 10.1115/1.4052402.

[37] J. D. Denton. "Loss Mechanisms in Turbomachines". In: vol. 2: Combustion and Fuels; Oil and Gas Applications; Cycle Innovations; Heat Transfer; Electric Power; Industrial and Cogeneration; Ceramics; Structures and Dynamics; Controls, Diagnostics and Instrumentation. ASME 1993 International Gas Turbine and Aeroengine Congress and Exposition. Cincinnati, Ohio, USA, May 24, 1993. DOI: 10.1115/93-GT-435.

[38] G. J. Gassner and A. D. Beck. "On the accuracy of high-order discretizations for underresolved turbulence simulations". In: *Theoretical and Computational Fluid Dynamics* 27.3 (June 2013), pp. 221–237. DOI: 10.1007/s00162-011-0253-7.

[39] B. Muth, M. Schwarze, R. Niehuis, and M. Franke. "Investigation of CFD Prediction Capabilities for Low Reynolds Turbine Aerodynamics". In: *Volume 7: Turbomachinery, Parts A and B*. ASME Turbo Expo 2009: Power for Land, Sea, and Air. Orlando, Florida, USA: ASMEDC, pp. 875–884. ISBN: 978-0-7918-4888-3. DOI: 10.1115/GT2009-59306.

[40] C. Müller-Schindewolffs, R.-D. Baier, J. R. Seume, and F. Herbst. "Direct Numerical Simulation Based Analysis of RANS Predictions of a Low-Pressure Turbine Cascade". In: *Journal of Turbomachinery* 139.8 (Mar. 2017). DOI: 10.1115/1.4035834.

[41] C. Morsbach, M. Bergmann, A. Tosun, B. F. Klose, E. Kügeler, and M. Franke. "Large Eddy Simulation of a Low-Pressure Turbine Cascade with Turbulent End Wall Boundary Layers". In: *Flow, Turbulence and Combustion* 112.1 (Jan. 2024), pp. 165–190. DOI: 10.1007/s10494-023-00502-6.

[42] N. A. Cumpsty and J. H. Horlock. "Averaging Nonuniform Flow for a Purpose". In: *Journal of Turbomachinery* 128.1 (Feb. 2005), pp. 120–129. ISSN: 0889-504X. DOI: 10.1115/1.2098807.

[43] F. Kock. "Bestimmung der lokalen Entropieproduktion in turbulenten Strömungen und deren Nutzung zur Bewertung konvektiver Transportprozesse". doctoral thesis. TU Hamburg-Harburg, 2003.

[44] F. Kock and H. Herwig. "Local entropy production in turbulent shear flows: a high-Reynolds number model with wall functions". In: *International Journal of Heat and Mass Transfer* 47.10 (2004), pp. 2205–2215. ISSN:

0017-9310. DOI: https://doi.org/10.1016/j.ijheatmasstransfer.2003.11.025.

[45] Y. Zhao and R. D. Sandberg. "Using a New Entropy Loss Analysis to Assess the Accuracy of RANS Predictions of an HPT Vane". In: vol. 2C: Turbomachinery. Turbo Expo: Power for Land, Sea, and Air. June 2019. DOI: 10.1115/GT2019-90126.

[46] T. Borcherding, C. Bode, M. Rosenzweig, P. J. Przytarski, J. Leggett, and R. D. Sandberg. "Entropy Loss Breakdown Comparison for LES and RANS of a Transonic Compressor Stage Midspan Section". In: vol. 13A: Turbomachinery — Axial Flow Fan and Compressor Aerodynamics. Turbo Expo: Power for Land, Sea, and Air. June 2023. DOI: 10.1115/GT2023-102949.

[47] D. Wilcox. *Turbulence Modeling for CFD*. Turbulence Modeling for CFD Bd. 1. DCW Industries, 2006. ISBN: 9781928729082.

[48] G. Raina, Y. Bousquet, D. Luquet, E. Lippinois, and N. Binder. "Loss Breakdown in Axial Turbines: A New Method for Vortex Loss and Wake Detection From 3D RANS Simulations". In: vol. 12C: Turbomachinery — Design Methods and CFD Modeling for Turbomachinery; Ducts, Noise, and Component Interactions. Turbo Expo: Power for Land, Sea, and Air. June 2024. DOI: 10.1115/GT2024-121181.